The Dynamics of Subglacial Plume Lift-off

Earle Wilson

December 18, 2019

1 Introduction

The melting of the Greenland and Antarctic ice sheets currently contributes approximately 1.1 mm per year of the total 3.3 mm per year rise in global sea-level [1]. Most notably, Greenland's contribution to this rate has increased more than 8-fold between 1994 and 2014 [2]. Recent studies have attributed the accelerated mass loss of the Greenland Ice Sheet to increased melting and ice loss at its marine interface [3–5]. Though much progress has been made to identify the primary mechanisms driving this enhanced mass loss, many aspects of this ice-ocean interaction remain poorly constrained. One such aspect is the impact of subglacial discharge.

Subglacial discharge refers to the release of meltwater from beneath the ice sheet into the ocean. This meltwater enters the ocean from the grounding line and rises along the face of a glacier as a turbulent plume. The turbulent mixing that occurs along the plume's path enhances submarine melting, and such melting may also promote the calving of icebergs [6–9]. Recent modeling efforts have shown that the submarine melt rate along a glacier's front is sensitive to the spatial distribution of subglacial outlets [10, 11]. In particular, model results show that a distributed line plume can produce up to five times as much melting as a single point source with the same discharge [10]. Despite its importance, the near-terminus hydrology of marine terminating glaciers remains poorly constrained [12]. This is in no small part due to the immense difficulty of accessing these regions.

The purpose of this project is to further our understanding of near-terminus subglacial discharge by exploring its dynamics with simple models and lab experiments. Here, we focus our attention on the transition that occurs as meltwater exits a subglacial channel and begins to rise as a buoyant plume. We refer to this transition as subglacial plume lift-off. We are specifically interested in where this lift-off occurs as it defines the extent to which relatively warm seawater floods a subglacial channel. This will help us determine the geometry of a subglacial channel's outlet to the ocean.

In this report, we present simple models for subglacial plume lift-off in a rectangular channel. This is accompanied by results from a series of laboratory experiments that attempt to replicate the essential dynamics of plume lift-off. We conclude by using our results to speculate on the extent of seawater intrusion under real-world glaciers.

2 Theoretical Model for a Salt Wedge

2.1 The estuarine analogy

In the subglacial plume lift-off zone, cold, fresh subglacial water rises into warm, salty seawater. It is conceivable that, under the right conditions, this lift-off may occur deep inside the subglacial channel. In this scenario, the ocean floods into the subglacial channel and undercuts the glacier. We assume that the dynamics of such an intrusion is fundamentally similar to that of a salt wedge estuary. A salt wedge estuary forms when a fast flowing fresh river discharges into a saline ocean with weak tidal mixing [13]. In this case, the *salt wedge* refers to the intrusion of seawater inside an estuary and coincides with where the river outflow lifts off the seabed and flows over the ocean [14]. In our case, the salt wedge refers to the section of the subglacial channel that is filled with seawater. This is illustrated in Figure 1.

We note that the dynamics of a salt wedge is somewhat similar to that of a two-layer exchange flow. In a typical two-layer exchange flow, two fluid reservoirs of different densities exchange mass via a narrow channel [15, 16]. Within the exchange flow's channel, light fluid flows above dense fluid in opposite directions. However, the flow within a salt wedge system is mostly uni-directional as the saline lower layer only partially intrudes the channel and terminates at a front. We believe the dynamics of a subglacial system is more similar to that of a salt wedge than a two-layer exchange flow.

2.2 An idealized salt-wedge with no entrainment

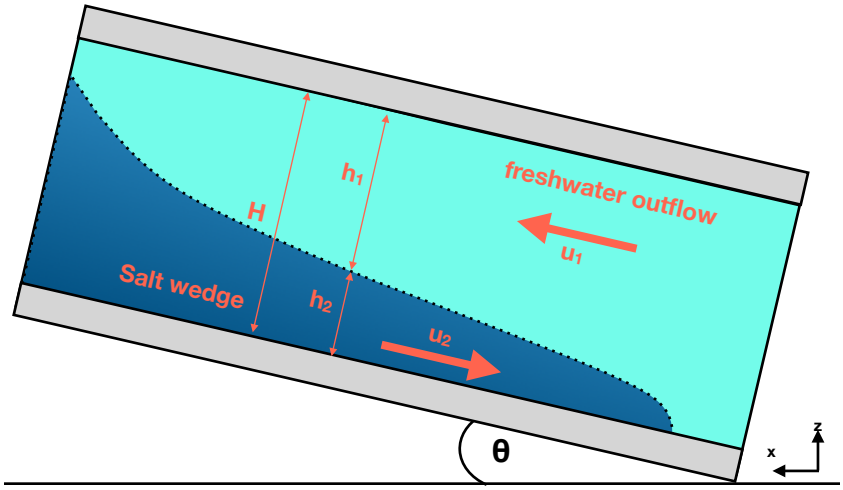

Figure 1: Schematic showing a cross-sectional view of a salt wedge in a rectangular channel

The schematic in Figure 1 illustrates an idealized salt wedge in a rectangular channel. Here, freshwater enters the channel from the right as salt water flows in from the left. The terms u_1 and u_2 are the along channel, layer averaged, velocities in the upper and lower layers, respectively.

To build our mathematical description of a subglacial salt wedge, we adapt the two layer salt wedge model presented in [17]. Like [17], we assume that the freshwater and salt water layers are well mixed and flow at a uniform speed. We likewise assume that the interface between the two layers is infinitely thin and features no interfacial mixing. However, unlike [17], which assumes a free upper surface for the top layer, we assume a rigid upper boundary to better represent the conditions within a subglacial channel. Additionally, we permit the channel to be tilted at a slight angle θ. Lastly, we restrict the height of the channel H to be constant but, for generality, permit its width w to vary.

Given the above assumptions, we can model this system using a pair of shallow water equations. With the stipulation of no entrainment, the continuity equations for the upper and lower layers are

$$w\,\frac{\partial h_1}{\partial t} + \frac{\partial Q_1}{\partial x} = 0, \tag{1}$$

$$w\,\frac{\partial h_2}{\partial t} + \frac{\partial Q_2}{\partial x} = 0. \tag{2}$$

Here, h_1 and h_2 are the thicknesses of the upper and lower layers, respectively. The thickness of the individual layers sum to give the height of the channel, H. Similarly, Q_1 and Q_2 are the volume fluxes of each layer, which in steady state are conserved along the channel. Continuing with our assumption of no entrainment, the momentum balance for both layers are given by

$$\frac{\partial u_1}{\partial t} + u_1\,\frac{\partial u_1}{\partial x} + \frac{\partial P}{\partial x} + \frac{C_i\,|u_1 - u_2|\,(u_1 - u_2)}{h_1} + C_d\,u_1^2\left(\frac{1}{h_1} + \frac{2}{w}\right) = 0 \tag{3}$$

$$\begin{aligned}\frac{\partial u_2}{\partial t} + u_2\,\frac{\partial u_2}{\partial x} + \frac{\partial P}{\partial x} + g'\left(\frac{\partial h_2}{\partial x} + \tan\theta\right) - \frac{C_i\,|u_1 - u_2|\,(u_1 - u_2)}{h_2} \\ + C_d\,u_2^2\left(\frac{1}{h_2} + \frac{2}{w}\right) = 0,\end{aligned} \tag{4}$$

where C_i and C_d are the coefficients for interfacial and wall drag, $\partial P/\partial x$ is the along channel pressure gradient, and g' is reduced gravity. In (3) and (4), we parameterize the interfacial and wall drag forces using the quadratic drag law. For interfacial drag, the transfer of momentum between the two layers is assumed to be proportional to the square of the difference between the layer-averaged velocities. For wall drag, the loss of momentum is assumed to be proportional to the square of the flow velocity that is adjacent to the wall. The $1/h_1$ and $1/h_2$ terms in (3) and (4) represent the scaling for drag along the top and bottom walls of the channel. The $2/w$ term is the corresponding scaling for drag along both side walls. If the width of the channel is much greater than its height, the effect of side wall drag is negligible.

Reduced gravity is defined as

$$g' = \frac{\Delta\rho}{\rho_0} g, \tag{5}$$

where $\Delta\rho$ is the density difference between the two layers, g is the acceleration due to gravity and ρ_0 is a reference density. If the temperature of the two layers are the same, $\Delta\rho/\rho_0$ may be approximated by

$$\frac{\Delta\rho}{\rho_0} = \beta\Delta S, \tag{6}$$

where ΔS is the salinity difference between the two layers and $\beta \sim 8 \times 10^{-4}$ PSU^{-1} is the haline contraction coefficient [17].

The along channel pressure gradient, $\partial P/\partial x$, serves a similar role to the hydrostatic pressure gradient induced by the sea surface slope gradient in a salt wedge estuary. In that system, the sea surface slopes downward towards the ocean and forces flow in the seaward direction. This is distinct from the force represented by $g'\left(\frac{\partial h_2}{\partial x}\right)$, which acts to drive flow that flattens the interface between the two layers.

To simplify the system, we assume a steady state where the freshwater volume flux, Q_1, is constant and the lower layer is stagnant ($u_2 = 0$). Furthermore, we assume that freshwater flow is always positive ($Q_1 > 0$). Additionally, we substitute the upper layer velocity u_1 in the momentum equations in favor of the upper layer volume flux by using the relationship $u_1 = Q_1/\, w\, h_1$, to obtain

$$\begin{aligned}\frac{Q_1^2}{w\,h_1}\frac{\partial}{\partial x}\left(\frac{1}{w\,h_1}\right) + \frac{\partial P}{\partial x} + C_i\left(\frac{Q_1}{w\,h_1}\right)^2\frac{1}{h_1} \\ + C_d\left(\frac{Q_1}{w\,h_1}\right)^2\left(\frac{1}{h_1} + \frac{2}{w}\right) = 0,\end{aligned} \tag{7}$$

$$\frac{\partial P}{\partial x} = C_i\left(\frac{Q_1^2}{w^2\,h_1^2 h_2}\right) - g'\left(\frac{\partial h_2}{\partial x} + \tan\theta\right), \tag{8}$$

where have used $h_2 = H - h_1$ for constant H. Combining the above equations and doing some algebra, we find

$$\begin{aligned}-\frac{Q_1^2}{g'w^2h_1^3}\left(\frac{\partial h_1}{\partial x} + \frac{h_1}{w}\frac{\partial w}{\partial x}\right) + C_i\frac{Q_1^2}{g'w^2h_1^2(H-h_1)} + \frac{\partial h_1}{\partial x} - \tan\theta \\ + C_i\,\frac{Q_1^2}{g'w^2\,h_1^3} + C_d\,\frac{Q_1^2}{g'w^2h_1^3}\left(1 + \frac{2h_1}{w}\right) = 0.\end{aligned} \tag{9}$$

At this stage, we define the non-dimensional upper layer Froude number as

$$Fr_1^2 = \frac{Q_1^2}{g'\,w^2\,h_1^3} = \frac{u_1^2}{g'h_1}. \tag{10}$$

By this definition, the upper layer Froude number varies in the along channel direction as h_1 and u_1 vary. When $Fr_1 = 1$, the flow is said to be *critical*. Flows for which $Fr_1 > 1$ and $Fr_1 < 1$ are classified as supercritical and subcritical, respectively. We also define the Froude number for the special case where $h_1 = H$ as

$$Fr_0^2 = \frac{Q_1^2}{g'\,w^2\,H^3} = Fr_1^2\left(\frac{h_1}{H}\right)^3. \tag{11}$$

Fr_0 is known as the *freshwater Froude number* [17]. Using (10), we re-write the previous equations as

$$(Fr_1^2 - 1)\frac{\partial h_1}{\partial x} = Fr_1^2 \left[C_i \left(\frac{H}{H - h_1} \right) + C_d \left(1 + \frac{2h_1}{w} \right) - \frac{h_1}{w} \frac{\partial w}{\partial x} \right] - \tan\theta. \tag{12}$$

The above equation describes the shape of a steady, non-entraining salt wedge in a rectangular channel, with variable width w and constant tilt θ. To gain some insight, we first consider the simpler case of a horizontal channel ($\theta = 0$) with constant width, for which

$$(Fr_1^2 - 1)\frac{\partial h_1}{\partial x} = Fr_1^2 \left[C_i \left(\frac{H}{H - h_1} \right) + C_d \left(1 + \frac{2h_1}{w} \right) \right]. \tag{13}$$

The salt wedge is defined as the distance between the freshwater lift-off point (i.e. the nose of the wedge) and the point at which $Fr_1 = 1$. For convenience, we designate $x = -L$ as the freshwater lift-off point and $x = 0$ as the point where the flow becomes critical. In this framework, the length of wedge is given by L. Additionally, $Fr_1 = 1$ at $x = 0$ and $Fr_1 = Fr_0$ at $x = -L$. To obtain the full shape of the wedge, we begin our integration of (13) from the point of critical flow, at $x = 0$. Since $Fr_1 = 1$ at $x = 0$, this determines h_1 at that boundary[1]. The integration is carried out in the negative x-direction (towards the freshwater source) until $h_1 \approx H$. Through this process, we can determine the freshwater liftoff point and the length of the salt wedge L.

Since the terms on the right of (13) are always positive, supercritical flow in the upper layer results in $\partial h_1/\partial x$ being positive. This means the freshwater layer will expand upon encountering the salt wedge and continue to do so until it becomes subcritical. However, if $Fr_0^2 > 1$, subcritical flow cannot occur within the channel. Therefore, a salt wedge cannot exist in a flat, uniform channel where $Fr_0^2 > 1$. If the upper layer flow is subcritical ($Fr_1^2 < 1$ and thus $Fr_0^2 < 1$), (13) predicts that the upper layer will decrease in height upon encountering the salt water layer. Unlike the supercritical case, this is conducive to a tw-layer flow and potentially a salt wedge.

If h_1 decreases indefinitely in the downstream direction, there must be a point along the channel where $Fr_1^2 = 1$. However, at this point, (13) becomes singular and thus appears to preclude the existence of such a flow. This apparent paradox can be avoided if we return to the more general case of a channel with variable width. If the width of the channel expands in the downstream direction, it is possible for the right of (12) to sum to zero. If that is case, the flow becomes critical wherever $(h_1/w)\,(\partial w/\partial x)$ balances the other terms in (12). More importantly, this permits the formation of a salt wedge. Alternatively, we can avoid this breakdown of our model by specifying that $Fr_1 = 1$ at the mouth of the channel, thereby establishing a hydraulic control at $x = 0$.

To summarize, a steady salt wedge can only occur if the flow in the freshwater layer is subcritical. Furthermore, for a salt wedge to occur in a horizontal rectangular channel with uniform cross-section, critical flow must occur outside the channel. More generally, critical flow can only be supported by a change in channel geometry.

[1]For practical purposes, we set $Fr_1 = 1 - \epsilon$ at $x = 0$ to avoid the singularity associated with critical flow. For these simulations, $\epsilon = 10^{-4}$.

Figure 2 shows solutions of equation 12 for a 10m channel with various freshwater flow velocities. The stated flow velocities are the freshwater flow rates that are imposed at the $x = -L$ boundary, where the plume lifts off the channel. The parameters used for this integration reflect that of a shallow estuary. Here, it is assumed that the width of the channel is much greater than its height and that there is no drag along the upper surface. Following [17], we set $C_i = 10^{-4}$, which is a value that is typical of salt-wedge estuaries.

Though this example is somewhat contrived, it allows us to visualize some key features of a salt wedge. In Figure 2, we see that the slope of the interface is steepest at both ends where $h_1 \approx H$ and $h_1 \approx 0$. This is expected since $h_1 = 0$ and $h_1 = H$ are singularities in equation 12. Additionally, Figure 2b suggests an inverse relationship between the freshwater flow speed and the equilibrated wedge length.

For the parameters chosen in this example, the wedge length is much longer than its height. However, this aspect ratio is set by the interfacial drag coefficient, which in this case is 10^{-4}. More generally, the wedge aspect ratio is dependent on some combination of the interfacial and wall drag coefficients, which are generally not known.

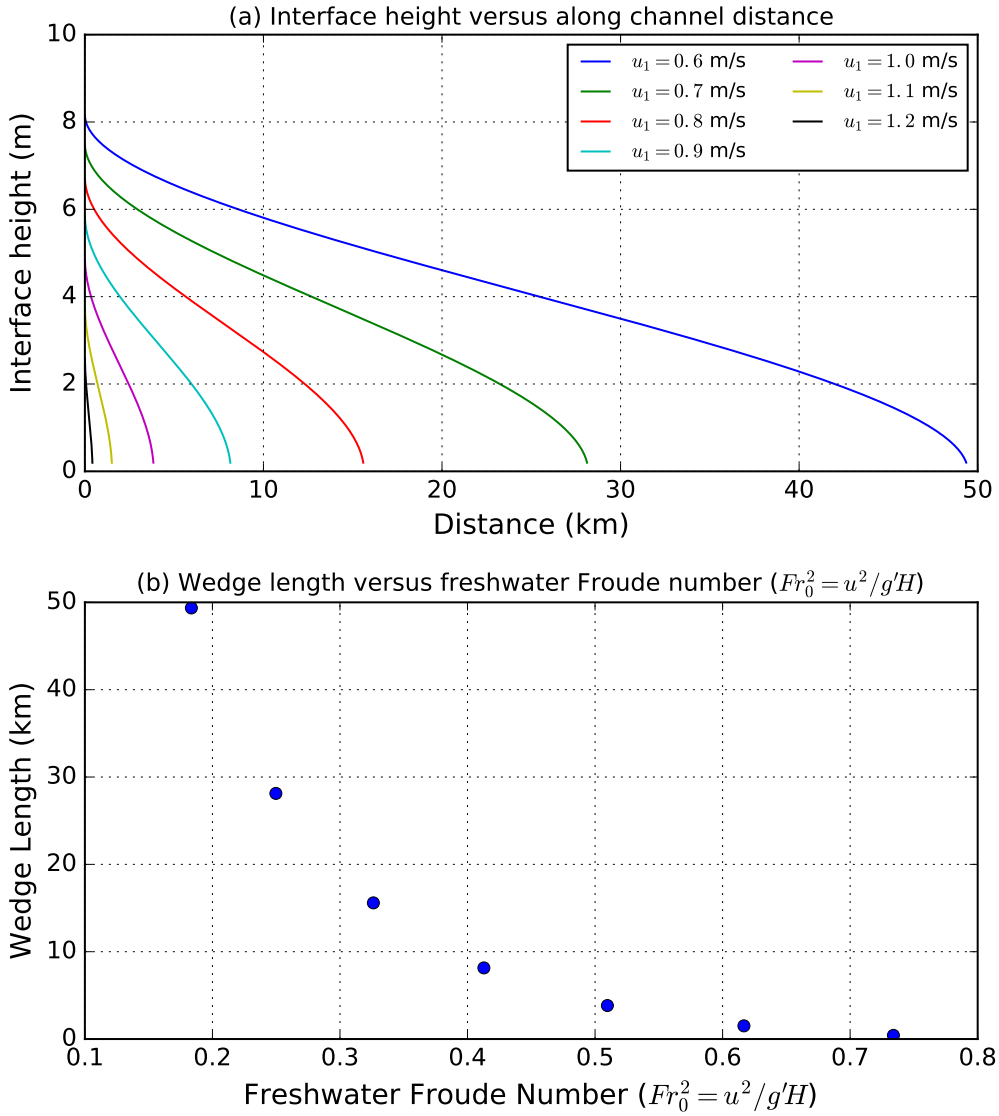

Figure 2: (a) Numerical solutions of equation 12 for a flat estuarine channel with various freshwater flow rates imposed at $x = -L$. For this example, $H = 10$m, $g' = 0.25$ ms^{-2} and $C_i = 10^{-4}$. The value $g' = 0.25$ corresponds to a freshwater and saltwater layer with salinities of 0 PSU and 25 PSU respectively. (b) Wedge length versus freshwater Froude number for the solutions shown in the top plot.

3 Laboratory Experiments

3.1 Experimental set-up

The main goals of these laboratory experiments are to test the theory outlined in the previous section and to obtain a scaling relationship that allows us to predict the extent of seawater intrusion in a hypothetical subglacial channel. Figure 3 provides a schematic of

our

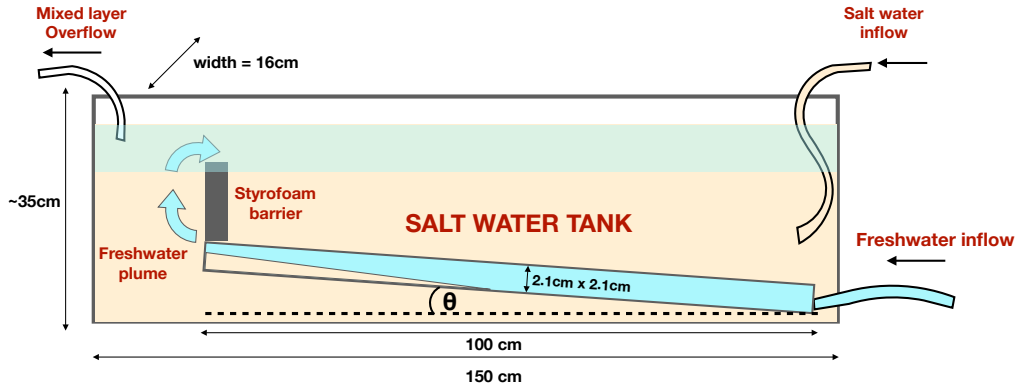

Figure 3: A schematic detailing the salt wedge experiments.

For all experiments, freshwater was pumped through a narrow rectangular duct into a much larger tank filled with saline water. The salt water tank was approximately 150 cm long, 16 cm wide and 35 cm deep The rectangular duct/channel was approximately 100 cm long and had an inner cross-section of 2.1 x 2.1 cm^2. This experimental configuration chosen so that a steady salt wedge would develop within the rectangular channel for the range of flow rates that could be supplied by the freshwater pump.

For these experiments, there were three main control parameters: the freshwater flow rate, the salinity of the main tank and the slope of the rectangular channel. The freshwater flow rated was varied using an adjustable pump over an approximate range of 5-30 cm^3/s. After careful calibration, this allowed us to precisely set the volume flux of freshwater into the tank. The tank or ambient salinity was varied by mixing local seawater ($\sim$33 PSU) with various amounts of freshwater. The tube slope was adjusted via a simple pulley system.

If we define the Reynolds number as

$$Re = \frac{uH}{\nu}, \tag{14}$$

where u is the imposed freshwater velocity prior to lift-off, H is the height of the channel and $\nu = 10^{-6}$ m^2/s is the kinematic viscosity. The imposed flow rate of 5-30 cm^3/s corresponds to a Re range of 250-1400.

Once set, the freshwater flow rate and tube slope remained fixed during an experiment. However, over the course of an experiment, a mixed layer would form at the top of the tank and grow overtime. To minimize the impact of this dilution, experiments were terminated when the depth of the diluted mixed layer grew to fill the upper two-thirds of the tank. To delay the recirculation of this diluted water to the opening of the rectangular channel, a styrofoam block was inserted above the channel's outlet. This styrofoam block was approximately 10cm high and spanned the width of the tank to form a partial dam.

To maintain a constant water level within the tank, a siphon into the mixed layer. In some runs, the salt water within the tank was replenished via a pump that was connected to a larger salt water reservoir. By tuning the siphon's drainage rate and salt water inflow rate,

it was possible to maintain a quasi-steady mixed layer depth and thus maintain constant ambient salinity at the level of the rectangular channel for an extended period of time.

3.2 Experimental procedure and data processing

The first set of experiments were conducted with the tank filled with seawater and the rectangular channel in a horizontal position ($\theta = 0$). With the freshwater pump turned on, the flow rate was held constant until a salt wedge appeared and visibly came to rest within the channel. Once that was realized, the flow rate was adjusted and held constant until the salt wedge evolved to a new equilibrium. This was repeated several times and came to end when the surface mixed layer began to encroach the lower third of the tank. At the end of an experimental run, the tank was drained then refilled with salt water for the next experiment.

A second set of experiments was conducted using seawater mixed with different amounts of freshwater to produce solutions with salinities that range from 16-33 PSU. A third set of experiments was conducted with the channel tilted at small positive angles as indicated in Figure 3.

Each experiment was video recorded with a digital camera that was mounted on a tripod facing the tank. The camera height was adjusted so that it was approximately level with the channel. To highlight the interface between the two layers, the inflowing freshwater was dyed blue and the tank was backlit by a diffuse light source. An image of the salt wedge, as observed during an experiment, is provided in Figure 4.

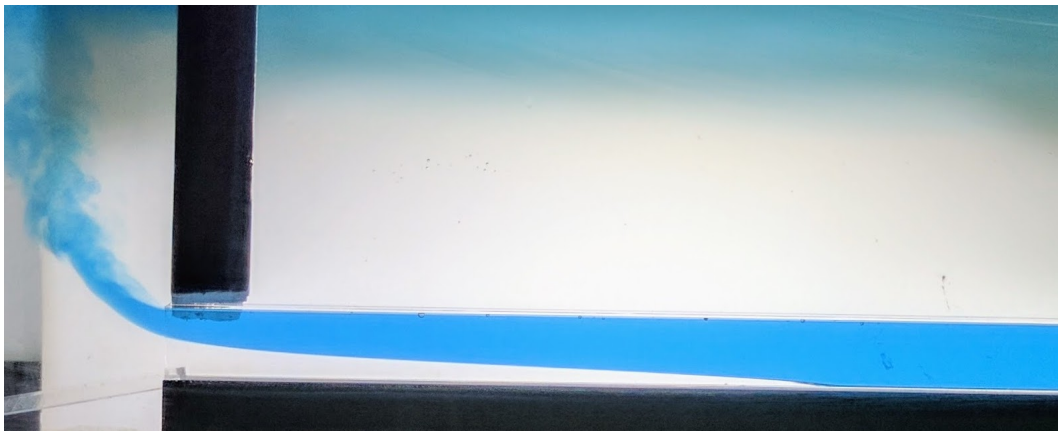

Figure 4: A closeup image of a part of the rectangular channel during an experiment. Here, a salt wedge is observed in the lower half of the tube. For reference, the height of the tube is 2.1 cm

To obtain quantitative data from these experiments, the video recordings were converted to a series of images sampled at every second. To identify the interface between the layers, the images were analyzed through their red channel. Since the dyed water was almost completely opaque to red light, the red channel provided the sharpest contrast between the two layers - much more so than the green and blue channels. This contrast was exploited through the use of a simple red-light intensity threshold. This thresholding was applied to

vertical sections of the tube in the image. Starting from the saline layer at the base of the tube, the interface was taken to be wherever the red light intensity fell below 10% of its maximum value. The majority of this process was automated with a set routines written in Python.

4 Horizontal Channel Experiments

4.1 Results summary

Figures 5 - 6 show example results for a single experimental run. In this run, the freshwater inflow was gradually reduced in five steps. The leftmost, dark blue bold line in Figure 5 indicates the initial equilibrated wedge position. Subsequent bold lines indicate the wedge position just before the pump speed was adjusted. This shows that the image processing algorithm was able to cleanly resolve the shape of the wedge.

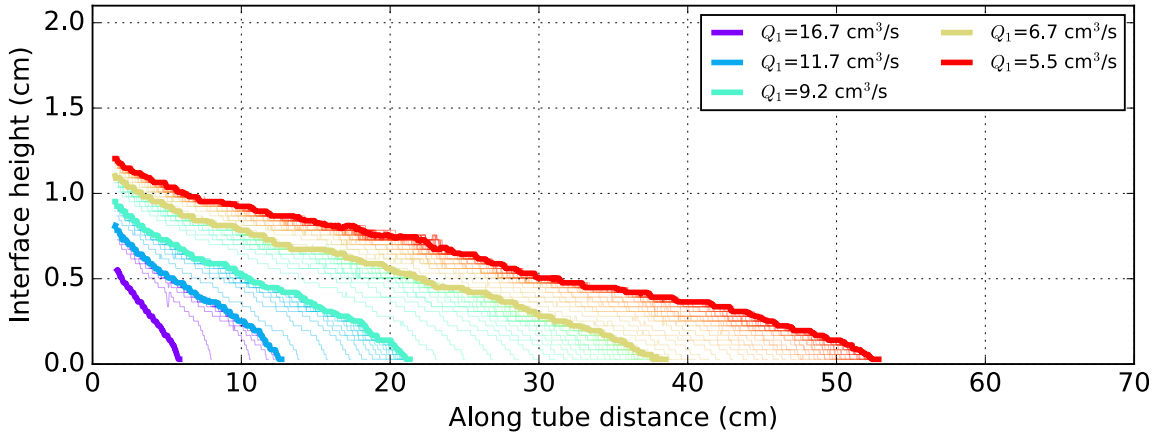

Figure 5: The evolution of a salt wedge for a horizontal channel experiment. Here, the freshwater volume flux was gradually reduced in five steps. Each line represents the position of the salt wedge interface at a 5 second interval. The bold lines indicate the final wedge position just before the freshwater volume was changed.

Figure 6a shows the evolution of the salt wedge length over the duration of the experiment. This plot confirms the salt wedge approached an equilibrium position before each step-change in the freshwater flow rate. In subsequent runs, this experiment was repeated in reverse to ensure that these longer wedge lengths did in fact reach their equilibrium positions. The right plot of Figure 6 shows the wedge length has an apparent inverse relationship with the freshwater volume flux. This relationship bears close resemblance to theoretical curve previously shown in Figure 2.

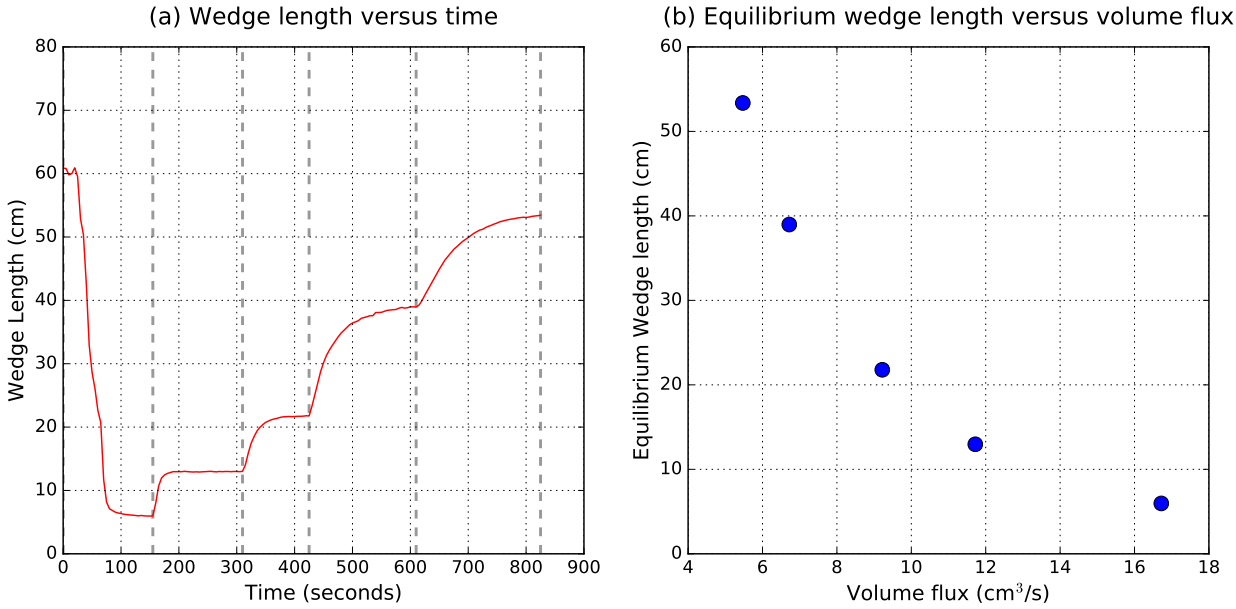

Figure 6: (a) Wedge length versus time for the volume fluxes shown Figure 5. The vertical dashed lines indicate when the freshwater flow rate was ramped down to a new value. (b) Equilibrated wedge length versus the freshwater volume flux.

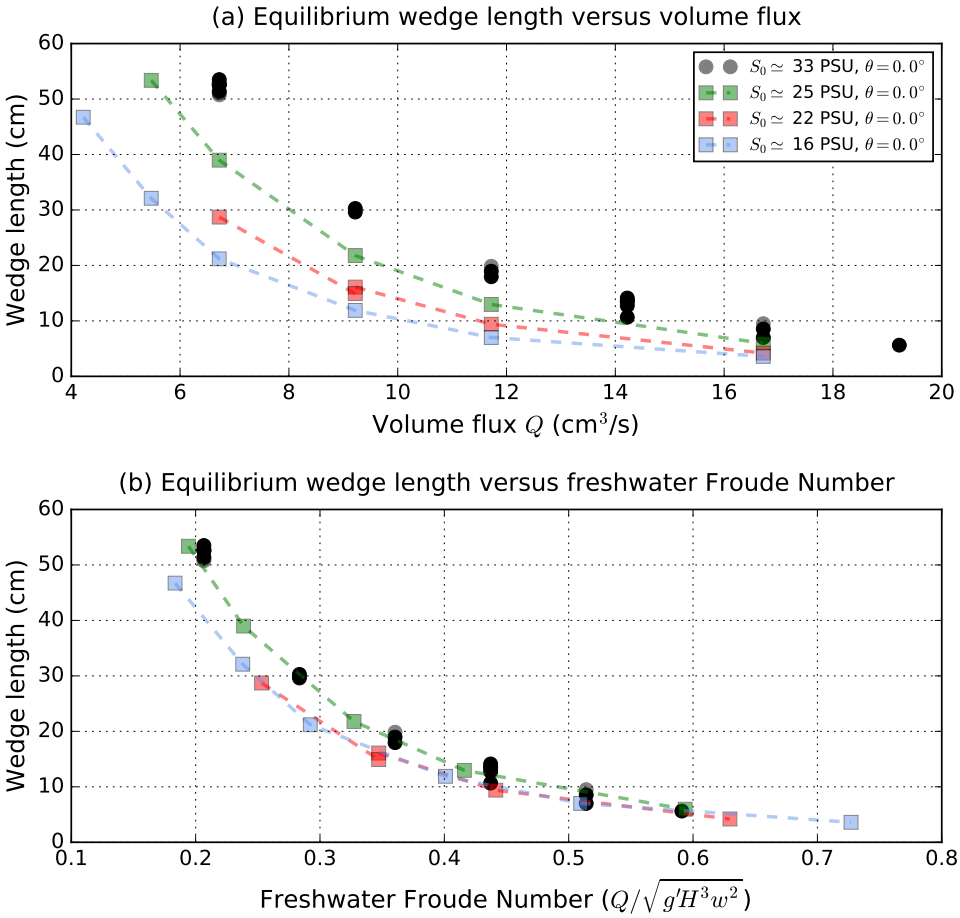

Figure 7: (a) Plot showing results for all horizontal channel experiments. Dark circles represent experiments with pure seawater. Colored squares represent experiments done with diluted seawater. Multiple data points are plotted for repeated runs. The ambient salinity S_0 for each experiment is provided in the legend. (b) Results for horizontal experiments rescaled in terms of the freshwater Froude number $Q^2/(g'H^3w^2)$.

Figure 7 shows the results for all horizontal channel experiments. Experiments with pure seawater are indicated by black circles. As indicated by the overlapping data points, most of these experiments were repeated several times at the same freshwater flow rate. The colored dots show results for runs done with diluted seawater. Three different seawater to freshwater ratios (3:1, 2:1 and 1:1) were used to produce tank salinities of 24.75 PSU, 22 PSU and 16 PSU. We observe that decreasing the tank salinity, and thus the density difference between the two fluids, reduces the length of the salt wedge for a given flow rate. This is consistent with our theory as reducing the density difference between the two layers is expected to reduce the tendency of the saline layer to slide under the fresh layer.

The effect of varying ambient salinity is mostly accounted for by rescaling the freshwater volume flux by each experiment's reduced gravity g'. This is shown in the lower plot of Figure 7, which compares the equilibrium wedge length with the non-dimensional freshwa-

ter Froude number. With this rescaling, the results mostly collapse along a single curve. However, we note that the runs done with the lower ambient salinities are still slightly offset from the other experiments. This slight discrepancy suggests the effect of varying the ambient salinity is not completely captured by g'.

4.2 Comparison with theory

Our next step is to compare the results described in the previous section with our theoretical expectations. The interface slope equation for a flat rectangular duct is given by (13) and is reproduced here for convenience

$$(Fr_1^2 - 1)\frac{\partial h_1}{\partial x} = Fr_1^2 \left[C_i \left(\frac{H}{H - h_1} \right) + C_d \left(1 + \frac{2h_1}{w} \right) \right].$$

From our experiment, we have direct measures of all values in the above equation except the wall and interfacial drag coefficients. Though there is a rich literature devoted to the wall drag experienced by single layer pipe flows [18–20], there is very little experimental precedent for the two-layer salt wedge system described here. Moreover, it is not immediately obvious that the wall drag scaling developed for single layer flow is appropriate for this particular two layer flow. Furthermore, we have no a priori knowledge for the value of the interfacial drag coefficient. Our recourse is to approximate these coefficients from the experimental data.

To accomplish this, we first reduce our number of unknowns to one by considering three limiting cases: $C_i = C_d$, $C_i = 0$ and $C_d = 0$. Next, we rescale the x-coordinate in our model such that $x = C_o\,\hat{x}$, where $C_o = C_i$ and/or $C_o = C_d$ depending the limiting case being considered. Doing this eliminates the drag coefficients from our model and gives

$$\frac{\partial h_1}{\partial \hat{x}} = \frac{Fr_1^2}{(Fr_1^2 - 1)} \left(1 + \frac{2h_1}{w} \right) \quad \text{for} \quad C_i = 0, \tag{15}$$

$$\frac{\partial h_1}{\partial \hat{x}} = \frac{Fr_1^2}{(Fr_1^2 - 1)} \left(\frac{H}{H - h_1} \right) \quad \text{for} \quad C_d = 0, \tag{16}$$

$$\frac{\partial h_1}{\partial \hat{x}} = \frac{Fr_1^2}{(Fr_1^2 - 1)} \left[\left(\frac{H}{H - h_1} \right) + \left(1 + \frac{2h_1}{w} \right) \right] \quad \text{for} \quad C_d = C_i. \tag{17}$$

For each case, we find solutions for the scaled wedge lengths $\hat{L}$ using the flow parameters from our experiments. With these theoretical wedge lengths, we then find C_o such that $L = C_o\,\hat{L}$. We accomplish this by performing a linear least-squares fit for each $\hat{L}$ versus L distribution. The result of this analysis is shown in Figure 8.

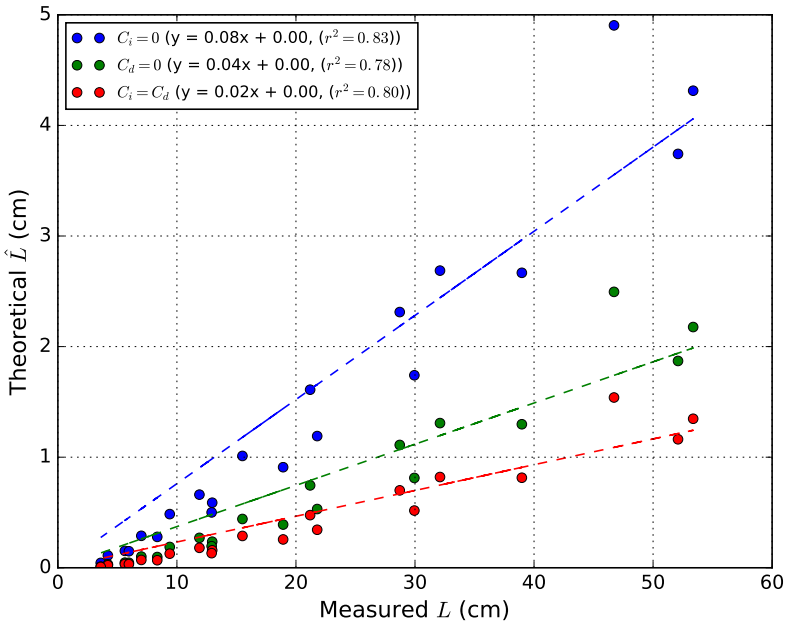

Figure 8: Plot showing scaled theoretical wedge lengths $\hat{L}$ versus experimental wedge lengths L for the three cases described by equations (15)-(17). The blue, green and red dots represent solutions for $\hat{L}$ assuming $C_i = 0$, $C_d = 0$, and $C_d = C_i$, respectively. The colored dashed lines represent the best fit line for each distribution. Here, the best fit line is forced to pass through $y = 0$.

The result of this analysis is shown in Figure 8, which plots the scaled theoretical wedge lengths $\hat{L}$, from equations (15)-(17), against their measured counterparts. Here, we have forced the best fit line to pass through $y = 0$. For each case, we see that the relationship between $\hat{L}$ and L is somewhat linear. The R-squared value for each fit is somewhat good ($R^2 \sim 0.8$) but the best fit lines generally lie above the data points associated with shorter wedges. This indicates that assuming $C_o\,\hat{L}$, where C_o is the slope of the best fit line, will generally underestimate the salt wedge length for higher flow rates or Froude numbers. Figure 9 shows that this is the case.

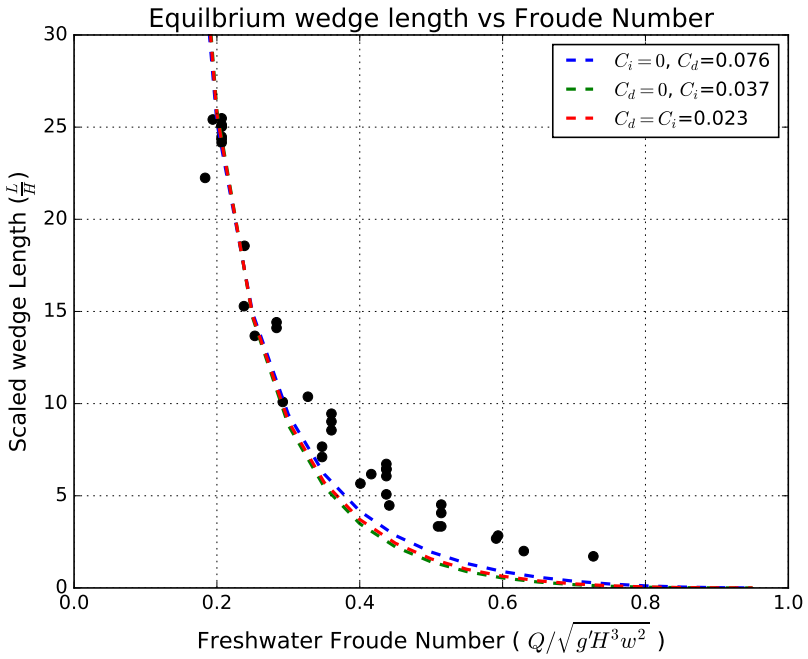

Figure 9: Data from Figure 7 overlain with theoretical curves for the three limiting cases described by (15)-(17). Here, the drag coefficients are assumed to be constant.

This discrepancy suggests that the relationship between $\hat{L}$ and L is not truly linear. A closer examination of Figure 8 reveals that the distribution of data points at shorter wedge lengths have a smaller slope than those at longer wedge lengths. Since shorter wedge lengths are associated with higher flow rates, this result suggest that the drag coefficients have an inverse relationship with the freshwater flow rate. This inverse relationship is well-established for the case of single layer pipe flow. For laminar flow pipe flow ($Re < 2000$), the Darcy friction factor f_D for wall drag is given by

$$f_D = \frac{64}{Re}, \tag{18}$$

where $f_D = 8\,C_d$ [18, 19]. This formulation suggests we should instead model our drag coefficients as

$$C_d = \frac{\tilde{C}_d}{Re}, \tag{19}$$

$$C_i = \frac{\tilde{C}_i}{Re}, \tag{20}$$

where is Re is given by (14). With this parameterization for the drag coefficients, we repeat the previous analysis now seeking values of $\tilde{C}_d$ and $\tilde{C}_i$ that best match our experimental data. For each case, our scaled salt wedge model is given by

$$\frac{\partial h_1}{\partial \hat{x}} = \frac{Fr_1^2}{(Fr_1^2 - 1)} \frac{1}{Re} \left(1 + \frac{2h_1}{w}\right) \quad \text{for} \quad \tilde{C}_i = 0, \tag{21}$$

$$\frac{\partial h_1}{\partial \hat{x}} = \frac{Fr_1^2}{(Fr_1^2 - 1)} \frac{1}{Re} \left(\frac{H}{H - h_1}\right) \quad \text{for} \quad \tilde{C}_d = 0, \tag{22}$$

$$\frac{\partial h_1}{\partial \hat{x}} = \frac{Fr_1^2}{(Fr_1^2 - 1)} \frac{1}{Re} \left[\left(\frac{H}{H - h_1}\right) + \left(1 + \frac{2h_1}{w}\right)\right] \quad \text{for} \quad \tilde{C}_d = \tilde{C}_i. \tag{23}$$

The result of this analysis is shown in Figure 10. In this case, the relationship between the scaled theoretical wedge lengths and the measured wedge lengths are well approximated by a straight line that pass through $y = 0$. Additionally, the quality of the line fits are significantly better ($R^2 > 0.9$). However, we note that in this case, $C_i = 0$ assumption produces a linear fit that is notably worse than the others. As expected, we see that the theoretical wedge lengths now have a much better agreement with the data (Figure 11).

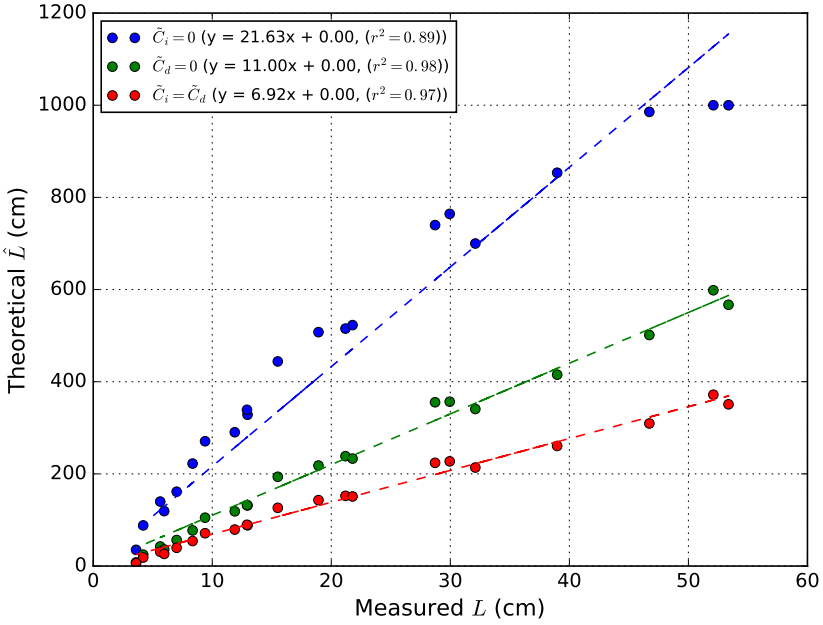

Figure 10: Like Figure 8 but now showing solutions for $\hat{L}$ for (21)-(23), which assume the drag coefficients are inversely proportional to Re.

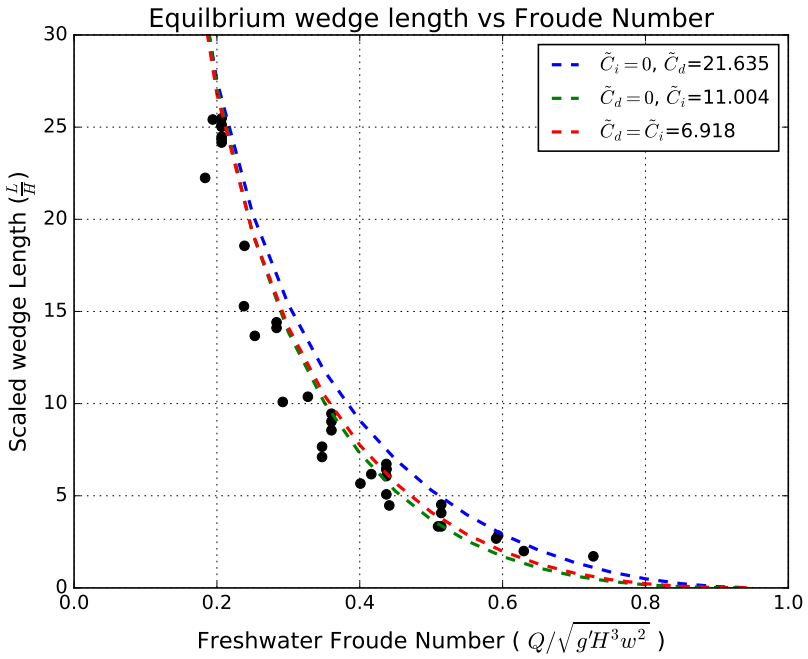

Figure 11: Data from Figure 7 overlain with theoretical curves for the three limiting cases described by (21)-(23). Here, the drag coefficients are assumed to be inversely proportional to Re.

From our regression analysis, we find that the $C_d = 0$ and $C_i = C_d$ scenarios produce theoretical wedge lengths that have equally good agreement with our data. When $C_i = C_d$, the best agreement is obtained when

$$C_i \;=\; C_d \;\approx\; \frac{7}{Re}. \tag{24}$$

This result is similar to the drag parameterization for laminar flow in a pipe [18]. We note that this result can only be validated for the range of Froude numbers we tested in the laboratory.

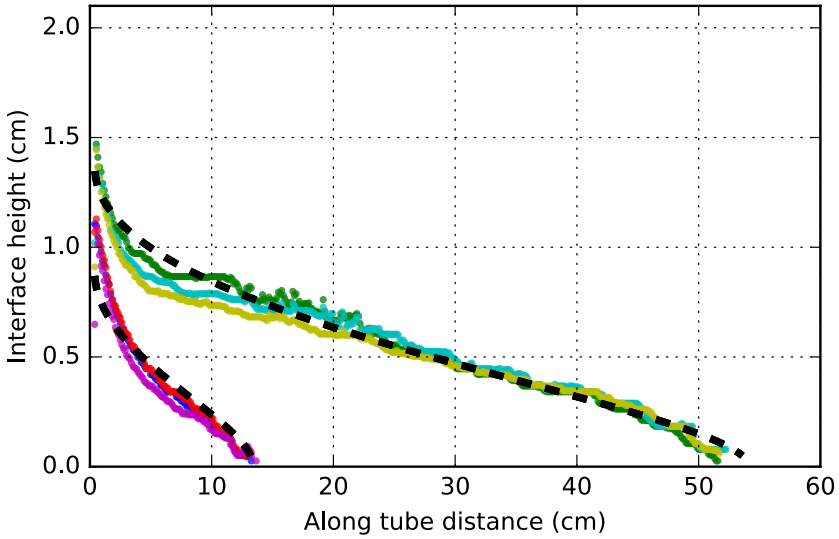

Figure 12: Comparisons between observed and theoretical wedge shapes. The observations are from a single run where the freshwater flow rate was varied back and forth between 6.7 cm^3/s and 14.2 cm^3/s. Data from the higher freshwater flow rate run are represented by the lower distribution of purple-red dots; the greenish dots represent the data for the higher flow rate. The black dashed lines represent the theoretical solution for each distribution. The theoretical wedge shapes were obtained by assuming $C_i = C_d \approx 7/Re$.

Next, we compare the shape of the observed salt wedge to that predicted by theory. Figure 12 shows direct comparisons between theoretical (black dashed lines) and observed (colored dots) interface shapes. The observations chosen here are for a single experimental run where the freshwater flow rate was varied between two flow rates that almost span the range of flow rates used throughout the experiments. In this example, we see that the observed wedge shapes agree reasonably well with our theoretical expectations.

5 Sloped Channel Experiments

5.1 Results summary

The experimental results described thus far have all been in the laminar regime ($Re \sim$ 250-1400). In each case, the interface between the salt and freshwater layers was always well defined and resembled the image shown in Figure 4. While this bodes well for our no-entrainment theory, the real subglacial system (with its much larger scales) is well within the turbulent regime. Thus, the final phase of this experiment, was an attempt to observe the salt wedge in a more turbulent state with significant interfacial mixing.

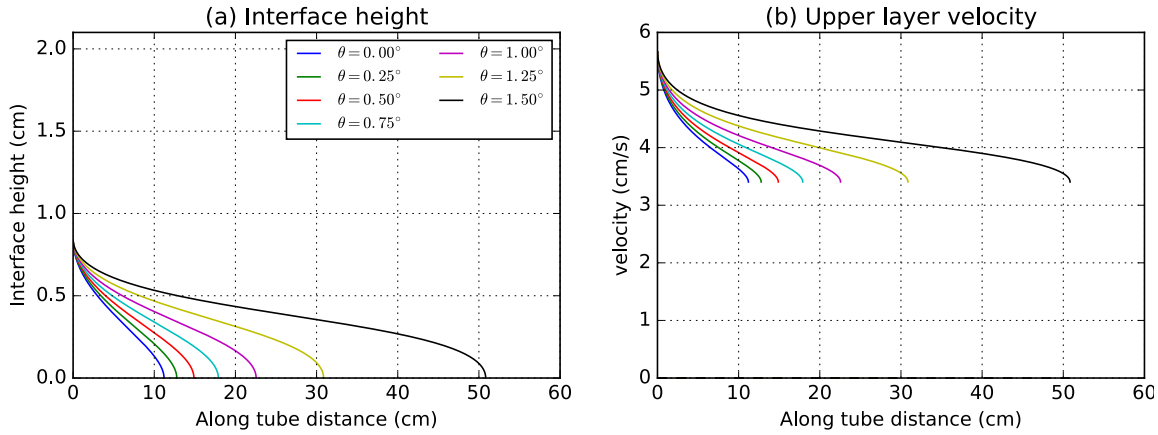

Figure 13: Solutions of (12) for a fixed freshwater flow rate at different channel slopes. For these simulations Q_1=15 cm^3/s, $H = w = 2.1$cm, g' = and $C_i = C_d \approx 7/Re$.

Given the narrow constraints of the rectangular channel and the limited range of the pump, the best way to achieve a state of significant interfacial mixing was to tilt the tube so that freshwater layer flowed upwards into the salt water tank. Introducing an upwards tilt allowed the freshwater layer to accelerate under the influence of its own buoyancy. This also introduced an additional tendency for the salt water layer to flow down slope into the channel. Together, both effects act to enhance the velocity shear across the interface ($(u_1 - u_2)/H$). This tendency is captured by the original theory as demonstrated in Figure 13.

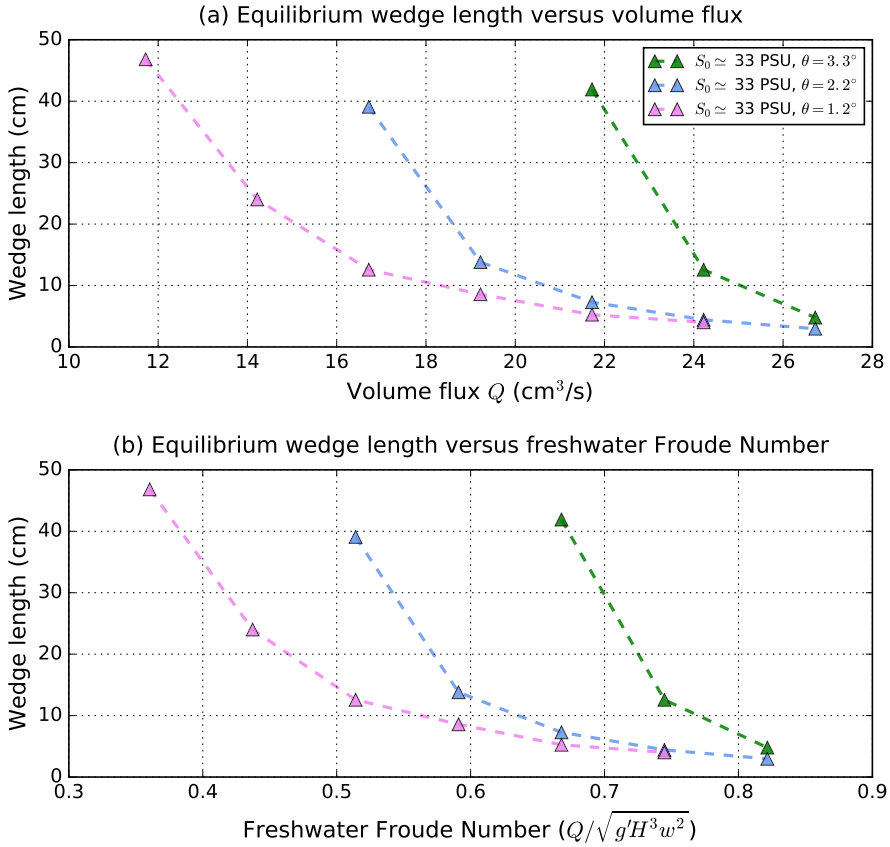

Figure 14: Equilibrium wedge length as in Figure 7, but for sloped channel experiments

Results for the sloped channel experiments are shown in Figure 14. As predicted by (12), increasing the channel slope produces longer salt wedges for a given flow rate. These results are for experiments conducted at relatively shallow channel slopes. At 3.3°, the steepest angle shown in Figure 14, the salt wedge still showed no signs of entrainment.

However, at slightly steeper channel slopes and higher freshwater flow rates, small amplitude interfacial waves began to appear. At even steeper slopes and higher freshwater flow rates, these interfacial waves grew and eventually began to overturn. At the steepest slopes obtained with the tank ($\theta \sim 8°$), the salt wedge transitioned into what visibly appeared to be an unsteady flow with significant interfacial mixing.

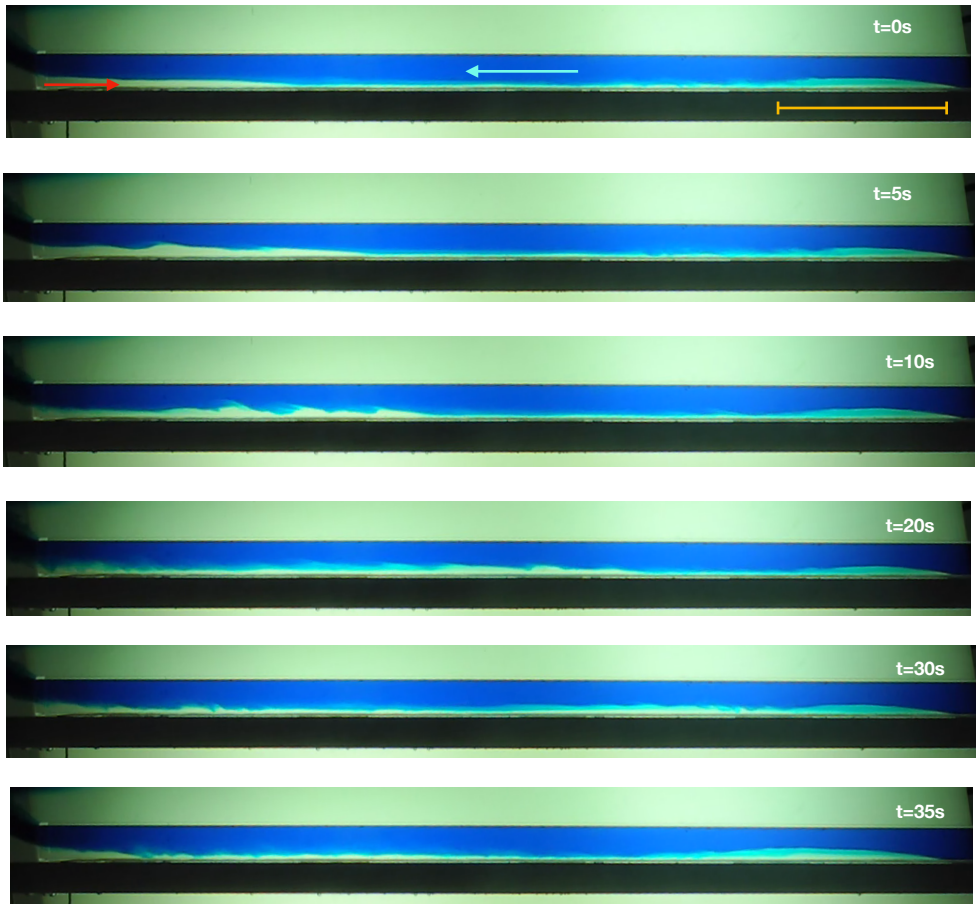

Figure 15: Rotated images showing the time evolution of interfacial waves inside a "steeply" sloped channel. For this experiment, the channel was tilted at 7.8° and the freshwater flow rate was set to 28 cm^3/s. In the top image, the red and blue arrows indicate the direction of the upper and lower layer flows while the orange bar shows the approximate position of the salt wedge.

Figure 15 shows rotated image snapshots of breaking interfacial waves in the wake of a salt wedge inside a channel tilted at 7.8°. For this run, the freshwater flow rate was held at 28 cm^3/s for just over 12 minutes. For the latter part of this run, the nose of the salt wedge occupied roughly the same position within the channel. During this period, the flow downstream of the salt wedge displayed episodic bursts of interfacial mixing, an example of which is presented in Figure 15.

At $t = 0$ seconds in Figure 15, the region downstream of the salt wedge was in a relatively quiescent state. Approximately five seconds later, a pulse of salt water entered the channel from the left. As this pulse of salt water travelled down the channel, it created wave-like disturbances that overturned and causing mixing across the interface ($t = 10 - 20$s). During this time, the salt wedge gradually contracted in size. The end result of this intense mixing was an intermediate layer of mixed fluid that continued to flow down the tube. At

$t = 35$s, the now diluted pulse of salt water replenished the salt wedge and the two layer flow returned to its initial quiescent state.

Such strong mixing episodes clearly violate the no-entrainment assumption used to build the earlier theory. We must therefore revise our theory to account for this new behavior.

6 Revised Theory for a Salt Wedge with Entrainment

6.1 Derivation

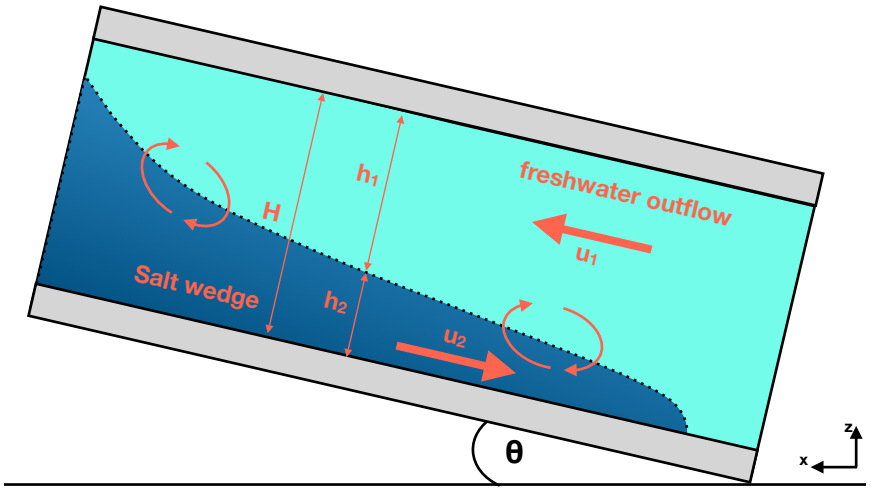

Figure 16: Schematic showing a cross-sectional view of a salt wedge in a sloped rectangular channel - now including entrainment.

With entrainment, the upper and lower layer continuity equations are given by

$$\frac{\partial h_1}{\partial t} + \frac{\partial q_1}{\partial x} = e, \tag{25}$$

$$\frac{\partial h_2}{\partial t} + \frac{\partial q_2}{\partial x} = -e, \tag{26}$$

where e is the entrainment rate, $q_1 = h_1\, u_1$ and $q_2 = h_2\, u_2$. The entrainment rate e has units of velocity and is parameterized in terms of the velocity difference between the layers

$$e = E\,(u_1 - u_2). \tag{27}$$

where E is an entrainment coefficient. Summing the continuity equations, we see that the total volume flux is conserved along the channel

$$q_1 + q_2 = q_0. \tag{28}$$

Likewise, salt conservation is given by

$$\frac{\partial}{\partial t}(S_1\, h_1) + \frac{\partial}{\partial x}\,(q_1\, S_1) = eS_2, \tag{29}$$

$$\frac{\partial}{\partial t}(S_2\, h_2) + \frac{\partial}{\partial x}\,(q_2\, S_2) = -eS_2, \tag{30}$$

where salinities within each layer, S_1 and S_2, are assumed to be uniform. Using (25) and (26), the salt conservation equation becomes

$$h_1\,\frac{\partial S_1}{\partial t} + q_1\,\frac{\partial S_1}{\partial x} = e(S_2 - S_1), \tag{31}$$

$$h_2\,\frac{\partial S_2}{\partial t} + q_2\,\frac{\partial S_2}{\partial x} = 0. \tag{32}$$

During entrainment, the upper layer expands and becomes more saline while the lower shrinks and maintains its salinity. In other words, entrainment is directed from the lower layer to the upper layer. Furthermore, S_2 is constant and determined by its value at the mouth of the channel.

As before, reduced gravity is given by

$$g' = \frac{\rho_2 - \rho_1}{\rho_0}\, g = \beta\,(S_2 - S_1)g \tag{33}$$

where β is the saline contraction coefficient. Using the above relation, we can re-write the upper layer salt budget as an equation for g'

$$h_1\,\frac{\partial g'}{\partial t} + q_1\,\frac{\partial g'}{\partial x} = -e\, g'. \tag{34}$$

The momentum conservation equations are given by

$$\frac{\partial u_1}{\partial t} + u_1\,\frac{\partial u_1}{\partial x} = \frac{G_1}{h_1} - C_d\, u_1^2\left(\frac{1}{h_1} + \frac{2}{w}\right) - C_i\,\frac{(u_1 - u_2)^2}{h_1} + \frac{e(u_2 - u_1)}{h_1}, \tag{35}$$

$$\frac{\partial u_2}{\partial t} + u_2\,\frac{\partial u_2}{\partial x} = \frac{G_2}{h_2} + C_d\, u_2^2\left(\frac{1}{h_2} + \frac{2}{w}\right) + C_i\,\frac{(u_1 - u_2)^2}{h_2}, \tag{36}$$

where

$$G_1 = -\,\frac{\partial P}{\partial x} - \rho_1\, g\, \tan\theta - \frac{1}{2}\, h_1\, \rho_1\, \frac{\partial g'}{\partial x}, \tag{37}$$

$$G_2 = -\,\frac{\partial P}{\partial x} - \rho_1\, g\, \tan\theta - \rho g'\left(\tan\theta - \frac{\partial h_1}{\partial x}\right). \tag{38}$$

These momentum equations are analogous to the ones introduced earlier for the no-entrainment case. Here, there are new additions that account for momentum exchange between the two layers due to entrainment and the fact that g' can now vary in the along channel direction.

After subtracting (36) from (35) and doing some simplifications, we arrive at

$$\begin{aligned}\frac{\partial}{\partial t}(u_1-u_2)+u_1\frac{\partial u_1}{\partial x}-u_2\frac{\partial u_2}{\partial x}=g'\left(\tan\theta-\frac{\partial h_1}{\partial x}\right)-\frac{1}{2}g'_x\,h_1\\ -C_d\left[\frac{u_1^2}{h_1}\left(1+\frac{2h_1}{w}\right)+\frac{u_2^2}{h_2}\left(1+\frac{2\,h_2}{w}\right)\right]-C_i\,(u_1-u_2)^2\left(\frac{1}{h_1}+\frac{1}{h_2}\right)-E\frac{(u_1-u_2)^2}{h_1}.\end{aligned} \tag{39}$$

The four main variables of interest are u_1, u_2, h_1 and g'. These variables can be evaluated using equations (25), (28), (34) and (39) provided the parameters q_0, θ, E, C_d and C_i are specified. In steady state, our four independent equations are

$$q_1+q_2=q_0, \tag{40}$$

$$\frac{\partial q_1}{\partial x}=E\,(u_1-u_2), \tag{41}$$

$$q_1\,\frac{\partial g'}{\partial x}=-E\,(u_1-u_2)\,g', \tag{42}$$

$$\begin{aligned}u_1\frac{\partial u_1}{\partial x}-u_2\frac{\partial u_2}{\partial x}=g'\left(\tan\theta-\frac{\partial h_1}{\partial x}\right)-\frac{1}{2}g'_x\,h_1-C_d\left[\frac{u_1^2}{h_1}\left(1+\frac{2h_1}{w}\right)+\frac{u_2^2}{h_2}\left(1+\frac{2\,h_2}{w}\right)\right]\\ -C_i\,(u_1-u_2)^2\left(\frac{1}{h_1}+\frac{1}{h_2}\right)-E\frac{(u_1-u_2)^2}{h_1}.\end{aligned} \tag{43}$$

For the sake of generality, we non-dimensionalize the above system of equations using the following scaling relationships: $x=L\hat{x}$, $h_1=H\hat{h}_1$, $h_2=H\hat{h}_2$, $w=H\hat{w}$, $u_1=U\hat{u}_1$, $u_2=U\hat{u}_2$, $g'=g'_o\hat{g}'$ and $q_1=HU\hat{q}_1$. Here, $H=h_1+h_2$ is the height of the channel and U is a characteristic velocity scale, which we define as $U=\sqrt{g'_0H}$. This allows us to state the upper and lower layer Froude numbers as

$$Fr_1^2=\frac{u^2}{g'h_1}=\frac{U^2\,\hat{u}^2}{g'_0H\hat{g}'\hat{h}_1}=\frac{\hat{u}_1^2}{\hat{g}'\hat{h}_1}, \tag{44}$$

$$Fr_2^2=\frac{\hat{u}_2^2}{\hat{g}'\hat{h}_2}. \tag{45}$$

In this non-dimensional framework, our system parameters can be written as

$$\tan\theta=\frac{H}{L}\hat{S}, \tag{46}$$

$$C_d=\frac{H}{L}\,\hat{C}_d, \tag{47}$$

$$C_i=\frac{H}{L}\,\hat{C}_i, \tag{48}$$

$$E=\frac{H}{L}\,\hat{E}, \tag{49}$$

$$q_0=\frac{\hat{q}_0}{H\,U}. \tag{50}$$

With these choice of scalings, our non-dimensional conservation equations have the exact form as the original dimensional equations ((40) - (43)). For the sake of convenience and at the risk of confusion, we now drop the hats off the non-dimensional variables.

Using $u_1 = q_1/h_1$ and $u_2 = q_2/h_2$, we re-write the momentum equations in terms of volume fluxes as

$$\begin{aligned}\left(\frac{q_1}{h_1^2}+\frac{q_2}{h_2^2}\right)\frac{\partial q_1}{\partial x}-\left(\frac{q_1^2}{h_1^3}+\frac{q_2^2}{h_2^3}-g'\right)\frac{\partial h_1}{\partial x} = g'S+\frac{1}{2}h_1\,\frac{q_0}{q_1^2}\,\frac{\partial q_1}{\partial x}\\ -C_d\left[\frac{q_1^2}{h_1^3}\left(1+\frac{2\,h_1}{w}\right)+\frac{q_2^2}{h_2^3}\left(1+\frac{2\,h_2}{w}\right)\right]-\left(\frac{C_i}{h_1h_2}+\frac{E}{h_1}\right)\left(\frac{q_1}{h_1}-\frac{q_2}{h_2}\right)^2.\end{aligned} \tag{51}$$

Here, we have made use of the fact that $h_1+h_2=1$ and $q_1+q_2=q_0$ in our non-dimensional framework. Additionally, by combining (41) and (42), we find

$$\frac{\partial}{\partial x}(q_1\,g') = 0. \tag{52}$$

This means the along slope buoyancy flux $q_1\,g'$ is conserved in this model. Moreover, from our definition of g', it follows that $g'=1$ upstream of the salt wedge where the freshwater layer fills the entire channel. Since the total volume flux is given by q_0, it follows that

$$g' = \frac{q_0}{q_1}. \tag{53}$$

With some rearrangement to (51), we can now completely outline our model for an entraining salt-wedge in a sloped channel as

$$h_1+h_2 = H = 1, \tag{54}$$

$$q_1+q_2 = q_0, \tag{55}$$

$$\frac{\partial q_1}{\partial x} = E\left(\frac{q_1}{h_1}-\frac{q_2}{u_2}\right), \tag{56}$$

$$\begin{aligned}\Gamma\frac{\partial q_1}{\partial x}-\left[Fr_1^2+Fr_2^2-1\right]\frac{\partial h_1}{\partial x} = S-C_d\left[Fr_1^2\left(1+\frac{2\,h_1}{w}\right)+Fr_2^2\left(1+\frac{2\,h_2}{w}\right)\right]\\ -\left(\frac{C_i}{g'h_1h_2}+\frac{E}{g'h_1}\right)\left(\frac{q_1}{h_1}-\frac{q_2}{h_2}\right)^2,\end{aligned} \tag{57}$$

where $\Gamma = \frac{1}{g'}\left(\frac{q_1}{h_1^2}+\frac{q_2}{h_2^2}-\frac{1}{2}\,\frac{h_1q_0}{q_1^2}\right)$. In the previous non-entraining case, the flow was critical when $Fr_1=1$. Here, critical flow occurs when the composite Froude number $G^2 = Fr_1^2 + Fr_2^2$ is unity. It should be noted that when $E=0$, equations (55)-(57) reduce to equation 13 - the original salt-wedge model that did not permit entrainment.

As before, $x=0$ is defined to be where the flow becomes critical, which here is where $G^2=1$. At the nose of the wedge, where $x=-L$, $h_1=1$ and $q_1=q_0$. In the non-entraining case, we found solutions for h_1 by starting our integrations at $x=0$, where $Fr_1^2=1$, and integrating in reverse until $h_1\approx H$. In that case, the critical point is associated with a unique value for h_1. However, in this case, there are many possible combinations of h_1 and

h_2 for which $G^2 = 1$. For this reason, we begin the numerical integrations at $x = -L$ where $h_1 = H^2$ and continue forward until $G^2 = 1$. Once this criteria is met, L can be determined.

6.2 Simulations

In this section, we present simulations of our revised salt wedge model that permits entrainment. For these simulations, we assume a rectangular channel with a 2.1 cm $\times$2.1 cm cross-section, similar to the one used in the laboratory experiments. At the boundary $x = -L$, the integrations were initialized with a 15 cm^3/s freshwater flux, which is again similar to what was used in some of the laboratory experiments. As described earlier, integrations were done in the positive x direction and came to end when $G^2 = 1$.

Following [6], we model the entrainment coefficient E as

$$E = E_o \sin\theta, \tag{58}$$

where θ is the slope of the channel and E_o is some constant. With this parameterization, entrainment is only permitted for non-zero channel slopes.

[2]Similar to the method for the non-entraining simulations, we specify $h_1 = H - \epsilon$ at $x = -L$ to avoid the singularity associated with zero lower layer thickness with $\epsilon = 10^{-4}$.

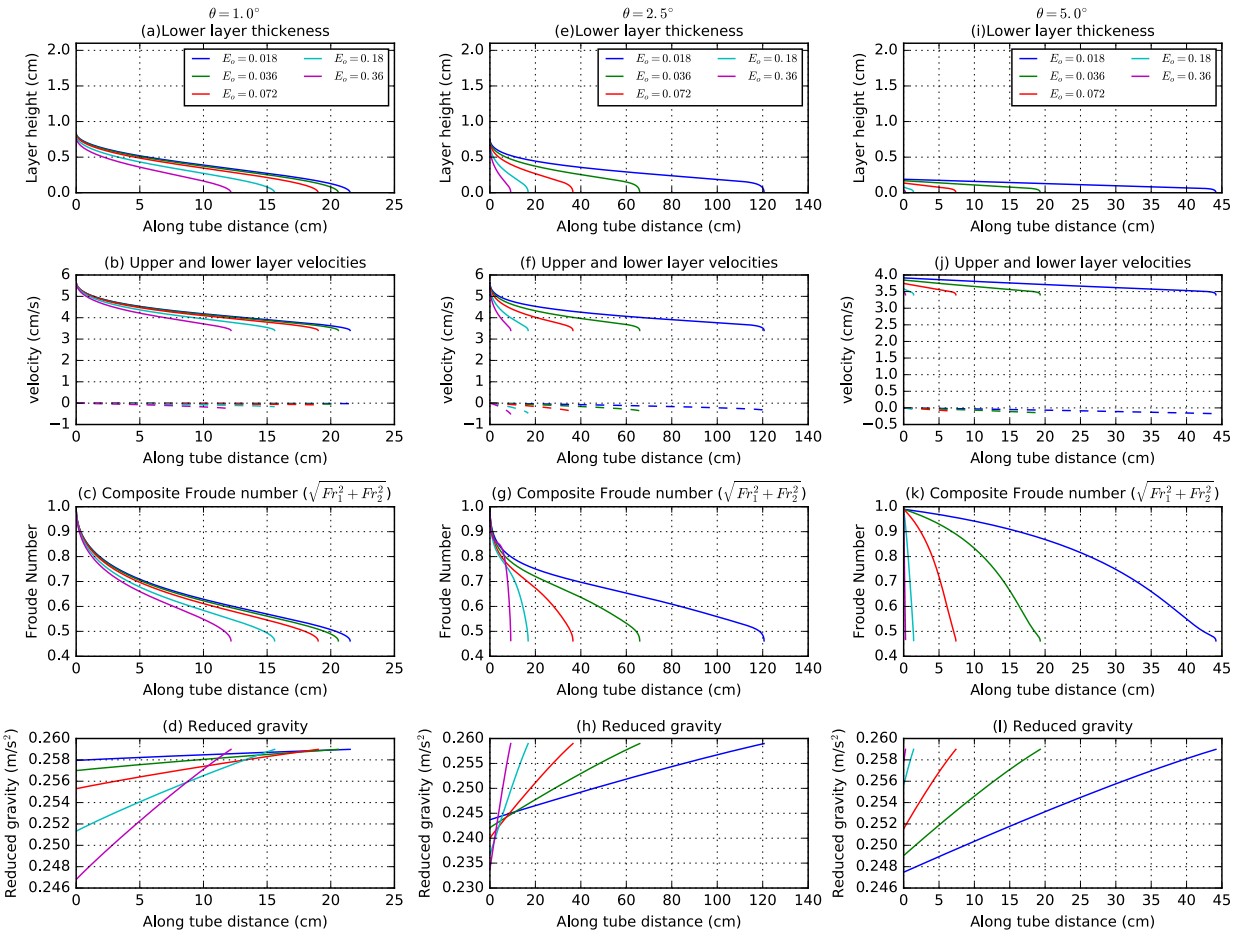

Figure 17: Figure showing solutions for the two-layer salt wedge model with entrainment for various channel slopes and entrainment coefficients. Rows: (From top to bottom) Solutions for along channel interface height, upper (solid lines) and lower (dashed lines) layer velocities, composite Froude number and reduced gravity. Columns: Solutions for various channel slopes θ. From left to right: $\theta = 1°$, $\theta = 2.5°$, $\theta = 5°$. These simulations were for a rectangular tube with a 2.1 cm $\times$2.1 cm cross-section. The upper layer flow was set to 15 cm^3/s at $x = -L$. Additionally, $C_i = C_d \approx 7/Re$.

Solutions for our two-layer salt wedge model for various channel slopes and entrainment coefficients are shown in Figure 17. Figure 17 a-d show simulations for various entrainment coefficients for a channel with a 1° slope. The values for the entrainment coefficients range from $E_o = 0.018$ to $E_o = 0.36$, corresponding to half and ten times the value used by [6].

In Figure 17a we observe that increasing the entrainment rate reduces the length of the salt wedge. This is because higher entrainment leads to a more rapid thinning and acceleration of the lower layer. Since the Froude number is inversely proportional to layer thickness, the acceleration of the initially thin lower layer drives a quick increase in the composite Froude number and thus a fast approach to critical flow (Figure 17 b-c). As expected, the reduced gravity decreases more rapidly in the along channel direction with

higher entrainment (Figure 17d).

Figure 17 e-h show similar results for a channel slope of 2.5°. In the non-entraining case, increasing the channel slope increases the length of the salt wedge for a given freshwater flux. Here, we observe that this response depends on the entrainment efficiency. For low entrainment efficiency, a steeper channel slope leads to a longer wedge (for example, the case for $E_o = 0.018$ in Figure 17 a, d), but at higher entrainment rates, a steeper channel can lead to a shorter wedge. The reason for this is two-fold. First, with our parametrization of entrainment (equation 58), increasing the channel slope results in a direct increase in the entrainment rate. Second, increasing the slope of the channel enhances the velocity shear across the two layers, which also enhances entrainment. Both effects tend produce shorter salt wedge intrusions due to their effect on the lower layer thickness and composite Froude number.

At $\theta = 5°$, we see the dominating effects of entrainment (Figure 17 i-l). The salt wedges produced by these simulations are all shorter and thinner than the previous cases. This behavior is again dominated by the rapid increase in Fr_2^2.

While these simulations are illuminating, they do not reproduce the initial expansion and subsequent contraction of the salt wedge downstream of its nose as shown in Figure 15. This points to several limitations of our salt wedge model. One reason for this discrepancy is that our salt wedge model has no time dependence. The mixing observed in the lab was driven by the intermittent breaking of interfacial waves. Therefore, accurate representation of this process may require a time dependent model. Second, our entrainment model assumes that momentum and mass from the lower is efficiently mixed throughout the upper layer. In contrast, the mixing observed in the laboratory was mostly concentrated near the two-layer interface. One could think of the laboratory observations as a case where the entrainment efficiency is relatively low. However, a more appropriate model for this type of mixing may be a three layer model, where entrainment results in the expansion of an intermediate layer with mixed fluid. Nevertheless, these simulations represent a significant improvement over the non-entraining model and will form the basis for future theoretical development.

7 Seawater Intrusions in a Realistic Subglacial Channel

As a final exercise, we use the salt wedge model developed in the previous section to predict the extent of seawater intrusions under real-world glaciers. For this exercise, we will assume a 10m by 10m channel that is oriented at a very shallow slope $\theta \leq 1$. For this channel, we find a range of subglacial discharge rates that produces freshwater Froude numbers Fr_0 between 0.2 and 0.9. Here, we note that our empirically derived drag coefficients are only valid for laminar flow and do not apply to this much larger system with $Re \sim 10^7$. From pipe flow theory, the wall drag coefficient is expected asymptote to some mean value (which will depend on wall roughness), rather than rapidly approach zero at very large Re [18]. As a matter of convenience, we simply assume $C_d = C_i = 7/1000$ - the approximate value for laminar flow when $Re = 1000$.

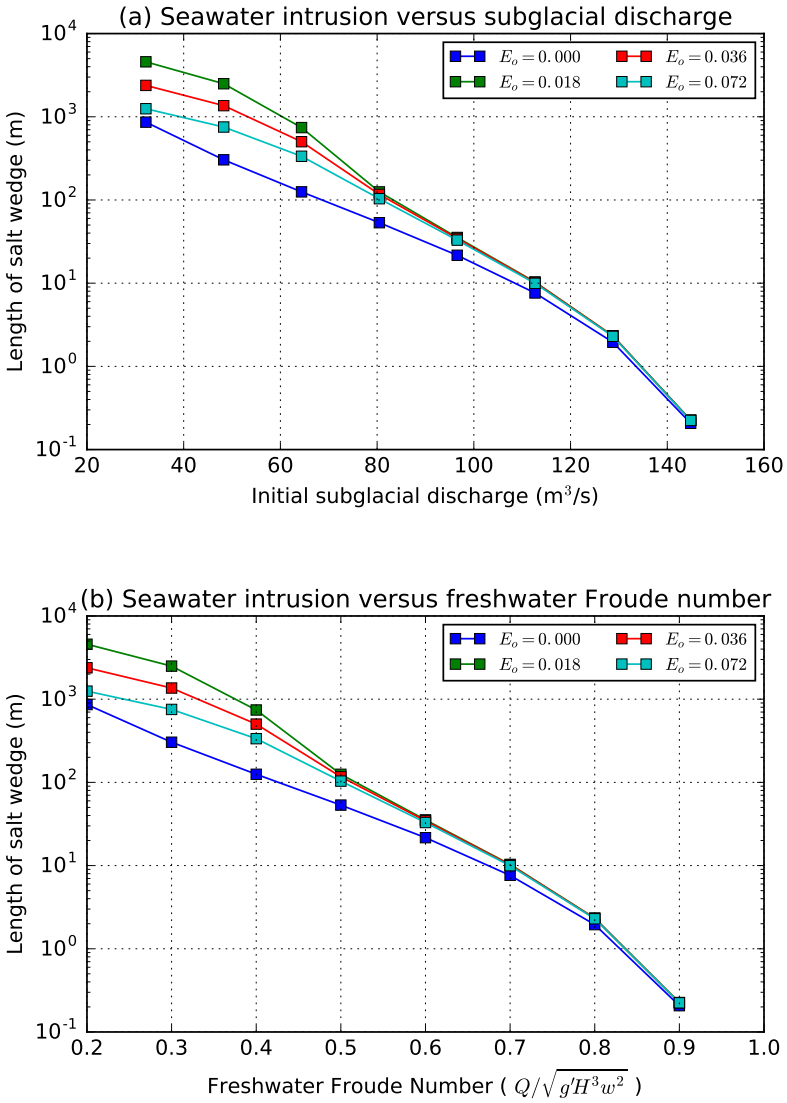

Figure 18: Solutions of salt wedge intrusions using parameters representative of a subglacial outlet. (a) Equilibrium salt wedge length versus subglacial discharge at $x = -L$ for different entrainment coefficients as represented by (58). (b) Equilibrium salt wedge length versus freshwater Froude number Fr_0. For this simulation, we assume a 10m by 10m subglacial channel and a range of subglacial discharge rates that produce Fr_0 values between 0.2 an 0.9. Since this system is well within the turbulent regime ($Re \sim 10^7$), we assume constant drag coefficients $C_d = C_i = 0.007$.

The results of this simulation are shown in Figure 18. Here, the equilibrium salt wedge length represents the extent of seawater intrusion into the subglacial channel. For a channel of this size, a Fr_0 range of 0.2 - 0.9 corresponds to a subglacial discharge range of approximately 30 m^3/s to 140 m^3/s. These values are consistent with parameters commonly used in axisymmetric plume models representing subglacial discharge in Greenland [10, 21].

For the imposed range of freshwater discharge Q, we see that the range of seawater intrusions span several orders of magnitude. For subglacial discharge above 100 m^3/s, the extent of seawater intrusion is minimal (less than a meter). For subglacial discharge below 50 m^3/s, the salt water intrusion extends hundreds of meters into the channel. This result suggests that subglacial channels with weak discharge likely have deep intrusions of seawater. Since the flooding of seawater will likely enhance melting within the subglacial channel, particularly along the lower walls that are in contact with the ocean, our results suggest that these channels will widen over time.

As the channel widens, our theory predicts even deeper seawater intrusions. For example, consider the the case $Q \approx 90$ m^3/s. For this channel geometry, $Fr_0 = 0.6$. In this state, the extent of seawater intrusion is only a few meters. However, a doubling of the channel's width results in a halving of the Fr_0. Assuming Q remains constant, the expected seawater intrusion is for $Fr_0 = 0.3$. From Figure 18b, we see that the length of this intrusion ranges from several hundred to several thousand meters - depending on the entrainment efficiency assumed.

Though this example is very idealized, it clearly illustrates the potential for salt wedges to greatly widen an initially narrow subglacial channel. These results appear to be consistent with recent field observations that suggest that subglacial discharge enters the ocean through broad line plumes rather than concentric point sources [9, 21]. However, we emphasize that these results are on a preliminary model and hinge on assumptions that are not completely justified. As stated in the previous section, our entraining salt wedge model does not accurately represent entrainment at steep channel relatively steep slopes. Additionally, our empirically derived drag coefficients are only valid for low Reynolds number flows.

8 Summary

In this study, we explored the dynamics of subglacial plume lift-off using a combination of idealized models and laboratory experiments. We developed our theoretical framework with the critical assumption that the subglacial flow system is fundamentally similar to that of a salt wedge estuary. With this understanding, we first formulated a theory that describes the steady-state properties of a non-entraining salt wedge confined to a rectangular channel. This theory predicts the shape and length of a salt wedge for a given freshwater volume flux, channel geometry and slope.

In parallel with this theoretical effort, we conducted a series of laboratory experiments to observe the behavior of a salt wedge in a rectangular channel. In these experiments, freshwater was pumped through a narrow rectangular tube into the bottom of tank, filled with water of higher salinity. Experiments were conducted with various freshwater flow rates, tank salinities and channel slopes. With the rectangular tube in a horizontal position, there were no visible signs of mixing across the salt wedge interface.

One key limitation of our salt wedge theory is that it relies on unconstrained coefficients for wall drag, C_d, and interfacial drag, C_i. These coefficients were ultimately determined by applying a least squares fit to the experimental data. From this analysis, we found that $C_d = C_i \approx 7/Re$ produced the best agreement between theoretical and observed wedge lengths (Figure 11). This result is only valid for the narrow range of laminar flow observed in our laboratory experiments.

Results from experiments conducted with small positive channel slopes (θ less than $\sim 3^\circ$) were qualitatively similar to those from the horizontal channel experiments. However, at steeper channel slopes, waves began to appear along the salt wedge interface. At the steepest channel slopes tested, the interfacial waves became unstable and caused mixing between the two layers (Figure 15). Since this observation violated our initial theoretical assumptions, an attempt was made to incorporate entrainment into our salt wedge theory.

This effort led to a revised salt wedge model that permitted the freshwater layer to acquire mass and momentum via entrainment of the more saline lower layer. A key assumption in this model is that both layers remain homogenous during and after entrainment. Following [6], the entrainment rate was assumed to be proportional to the shear across the salt wedge interface and the sine of the channel slope. With this revised salt wedge model, we find that increasing the entrainment rate leads to shorter salt wedges. At high entrainment rates, momentum is efficiently transferred from the upper layer to the lower layer. If the lower layer is initially thin, this results in a rapid increase in the lower layer Froude number and thus the composite Froude number. This was the case in our simulations since we began our integrations at the nose of the salt wedge, where the freshwater begins to lift off the base of the channel.

With our entraining salt wedge model, we speculated on the extent of seawater intrusions for a typical subglacial outlet system. Though these results are preliminary, we find that the extent of seawater intrusion into a subglacial channel can be quite significant and there is a strong tendency for the subglacial channel to expand laterally. This tendency for the subglacial system to form wide discharge outlets would be consistent with recent observations of broad line plumes at tidewater glaciers in Greenland [9, 21].

9 Future work

Though insightful, our revised model did not reproduce the observed thinning and subsequent expansion of the freshwater layer as it lifts off the channel and begins to entrain the lower layer (Figure 15). For future work, we propose further developing the two-layer salt wedge model to better represent our experimental results. One possible improvement to our model would be to introduce an intermediate layer along the salt wedge interface. Close observations of experiments done with a steeply sloped channel revealed that the entrainment was mostly confined to the interface. This is similar to what has been observed in exchange flow experiments [15, 16]. Furthermore, the transient mixing observed in some of our experiments seems to warrant a time-dependent salt wedge model.

A natural extension of our laboratory experiments would be to repeat them at a higher Reynolds number. Achieving full turbulence would almost certainly require a much larger experiment set-up. Doing this would allow for proper determination of the drag coefficients that better represent actual subglacial flow, which is highly turbulent.

10 Acknowledgements

First and foremost, I would like to express my deepest gratitude to my advisers Ian Hewitt, Andrew Wells and Claudia Cenedese. Without their expert guidance and countless hours of

assistance, this project would not have been possible. I would also like to extend a special thanks to Anders Jensen for helping to set up our laboratory experiment and providing technical support throughout the project. Lastly, I would like to thank the many students, fellows and staff of the GFD program who helped to make my time spent at Woods Hole an incredibly fun and intellectually stimulating experience.

References

[1] E. Rignot, J. Mouginot, and B. Scheuchl. Antarctic grounding line mapping from dif-ferential satellite radar interferometry. *Geophysical Research Letters* 38.10 (2011), doi: 10.1029/2011GL047109.

[2] X. Chen et al. The increasing rate of global mean sea-level rise during 1993–2014. *Nature Climate Change* 7.7 (2017), pp. 492–495. doi: 10.1038/nclimate3325.

[3] M. van den Broeke et al. Partitioning recent Greenland mass loss. *Science* 326.5955 (2009), pp. 984–986. doi: 10.1126/science.1178176.

[4] E. Rignot, M. Koppes, and I. Velicogna. Rapid submarine melting of the calving faces of West Greenland glaciers. *Nature Geoscience* 3.3 (2010), pp. 187–191. doi: 10.1038/ngeo765.

[5] F. Straneo and C. Cenedese. The dynamics of Greenland's glacial fjords and their role in climate. *Annual Review of Marine Science* 7.1 (2015), pp. 89–112. doi 10.1146/annurev-marine-010213-135133.

[6] A. Jenkins. Convection-driven melting near the grounding lines of ice shelves and tidewater glaciers. *Journal of Physical Oceanography* 41.12 (2011), pp. 2279–2294. doi: 10.1175/JPO-D-11-03.1.

[7] Y. Xu et al. Numerical experiments on subaqueous melting of Greenland tidewater glaciers in response to ocean warming and enhanced subglacial discharge. *Annals of Glaciology* 53.60 (2012), pp. 229–234. doi: 10.3189/2012AoG60A139.

[8] M. O'Leary and P. Christoffersen. Calving on tidewater glaciers amplified by submarine frontal melting. *The Cryosphere* 7.1 (2013), pp. 119–128. doi: 10.5194/tc-7-119-2013.

[9] M. J. Fried et al. Distributed subglacial discharge drives significant submarine melt at a Greenland tidewater glacier. *Geophys. Res. Lett.* 42 (2015), pp. 9328–9366. doi: 10.1002/2015GL065806.

[10] D. A. Slater et al. Effect of near-terminus subglacial hydrology on tidewater glacier submarine melt rates. *Geophysical Research Letters* 42.8 (2015), pp. 2861–2868. doi: 10.1002/2014GL062494.

[11] D. Carroll et al. The impact of glacier geometry on meltwater plume structure and submarine melt in Greenland fjords. *Geophysical Research Letters* 43.18 (2016), pp. 9739–9748. doi: 10.1002/2016GL070170.

[12] D. Slater et al. Spatially distributed runoff at the grounding line of a large Green-andic tidewater glacier inferred from plume modelling. *Journal of Glaciology* 63.238 (2017), pp. 309–323. doi; 10.1017/jog.2016.139.

[13] D. V. Hansen and M. Rattray. New dimensions in estuary classification. *Limnology and Oceanography* 11.3 (1966), pp. 319–326. doi 10.4319/lo.1966.11.3.0319.

[14] J. B. Schijf and J. C. Schonfeld. Theoretical considerations on the motion of salt and fresh water.Proceedings Minnesota International Hydraulics Convention, 1953.

[15] C. R. Meyer and P. F. Linden. Stratified shear flow: experiments in an inclined duct. *Journal of Fluid Mechanics* 753 (2014), pp. 242–253. doi: 10.1017/jfm.2014.358.

[16] A. Lefauve et al. Three-dimensional, time-resolved velocity and density measure-ments of the stratified shear flow in an inclined duct. *VIIIth International Symposium on Stratified Flows* (2016).

[17] W. Geyer and D. Ralston. The dynamics of strongly stratified estuaries. *Treatise on Estuarine and Coastal Science*. Elsevier, 2011. Chap. 2, pp. 37–51. doi: 10. 1016/B978-0-12-374711-2.00206-0.

[18] L. F. Moody. Friction factors for pipe flow. *Trans ASME* 66 (1944), pp. 671–684.

[19] N. H. Chen. An explicit equation for friction factor in pipe. *Industrial & Engineering Chemistry Fundamentals* 18.3 (1979), pp. 296–297. doi: 10.1021/i160071a019.

[20] B. J. McKeon et al. Friction factors for smooth pipe flow. *Journal of Fluid Mechanics* 511 (2004), pp. 41–44. doi 10.1017/S0022112004009796.

[21] R. H. Jackson et al. Near-glacier surveying of a subglacial discharge plume: Implications for plume parameterizations. *Geophysical Research Letters* 44.13 (2017), pp. 6886–6894. doi: 10.1002/2017GL073602.